

# Photonic Spin Hall Effect in a Four-Level Coherent Control Scheme within Cavity QED

Muzamil Shah,<sup>1,2</sup> Shahid Qamar,<sup>3,4</sup> and Muhammad Waseem<sup>3,4,\*</sup>

<sup>1</sup>*Department of Physics, Zhejiang Normal University, Jinhua, Zhejiang 321004, China*

<sup>2</sup>*Department of Physics, Quaid-i-Azam University, Islamabad 45320, Pakistan*

<sup>3</sup>*Department of Physics and Applied Mathematics,*

*Pakistan Institute of Engineering and Applied Sciences (PIEAS), Nilore 45650, Islamabad, Pakistan*

<sup>4</sup>*Center for Mathematical Sciences, PIEAS, Nilore, Islamabad 45650, Pakistan*

(Dated: November 27, 2024)

This paper investigates the manipulation of the photonic spin Hall effect (PSHE) using a four-level closed coherent control coupling scheme in cavity quantum electrodynamics (QED). The atomic system is configured to function as a combined Tripod and  $\Lambda$  (CTL), or  $\Lambda$ , or  $N$  level model by manipulating the control field strengths and their relative phases. The system demonstrates multiple transparency windows in the CTL configuration, allowing the tunable PSHE over the wider range of probe field detuning. At probe field resonance, the  $\Lambda$ -type system exhibits PSHE similar to the CTL system, showing enhanced PSHE due to zero absorption and dispersion. Control field strengths and atomic density show no influence on PSHE. Our findings reveal that atomic density and strength of control fields significantly influence PSHE in the  $N$ -type model at resonance, offering additional control parameters for PSHE manipulation. The results are equally valid and applicable to direct  $\Lambda$ -type and  $N$ -type atomic systems, making the findings broadly relevant in cavity QED. The demonstrated tunability via probe field detuning, control fields, and atomic density paves the way for advanced optical control and enhanced precision in cavity QED devices.

## I. INTRODUCTION

Originally, the Spin Hall Effect (SHE) arises in solid-state systems, where it refers to the transverse shift of particles (such as electrons) due to spin-orbit coupling [1, 2]. In these electronic systems, the spin-orbit interaction causes particles with spin-up and spin-down states to experience different transverse forces when moving through the electronic potential [3]. This results in a transverse displacement of the particles, which is known as the SHE [4]. The SHE has been widely studied in condensed matter systems such as semiconductors [5], graphene [6], topological insulators [2], and two-dimensional materials [7], where spin separation occurs due to intrinsic or induced mechanisms. Similarly, spin separation has been achieved through optically generated spin currents of exciton-polaritons in semiconductor microcavities, a phenomenon known as optical SHE [8].

On the other hand, the PSHE deals with the analogous behavior of photons in coherent light-matter interaction. In PSHE, right-circularly polarized and left-circularly polarized components play a role similar to spin-up and spin-down electrons. The refractive index gradient of the matter acts as an analog to the electronic potential. In PHSE, left-circularly polarized and right-circularly polarized photons experience different shifts perpendicular to the incident plane due to spin-orbit interaction as they interact with the interface of the coherent medium [9]. The PSHE is mainly attributed to the optical angular momentum and two geometric

phases [10]. One geometric phase is the spin-redirected Rytov-Vlasimirskii-Berry (RVB) phase associated with the propagation direction of the wave vector, and the second is the Pancharatnam-Berry (PB) phase related to the polarization manipulation of light [10, 11]. Recently, the PSHE gained particular attention for its ability to control spin-dependent behaviors of photons in various optical media. For example, semiconductors [12], graphene layers [13–15], surface plasmon resonance systems [16–20], metamaterials [21], all-dielectric metasurfaces [22], topological insulators [23], strained Weyl semimetals [24], hyperbolic metamaterials [25], and two-dimensional quantum materials [26, 27]. The PSHE has enabled applications such as probing topological phase transitions [26, 27], identifying graphene layers [13], chiral molecular detection [28], and performing mathematical operations and edge detection [29].

The PSHE traces back to the out-of-plane Imbert-Fedorov (IF) shift perpendicular to the incident plane [30]. The IF Shift can also be attributed to the spin-orbit interaction of light and is linked with the spin-redirected RVB phase [10, 11]. However, IF-Shift is formulated differently by considering right-circular polarized or left-circular polarized light at the optical interface. On the other hand, PSHE considers the incident linearly polarized beam as a superposition of the right-circular polarized and left-circular polarized components. Besides, an in-plane Goos-Hanchen (GH) shift to the incident plane at an optical interface originates from the spatial dispersion of beam reflection, transmission coefficients, and the interference of the angular spectrum components [31].

In quantum optics, atomic coherence effects of light-matter interaction have enabled groundbreaking discoveries, including electromagnetically induced trans-

\* mwaseem@pieas.edu.pk

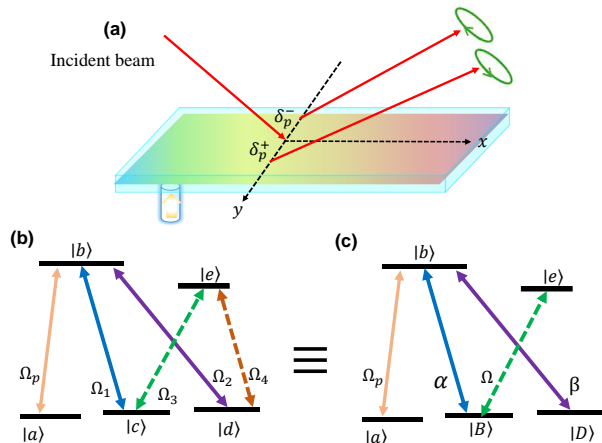


FIG. 1. (a) Schematic diagram of the physical model. The atomic sample from the bottom nozzle spreads into an ultra-high vacuum glass vapor cell made of Pyrex with inner thickness  $d = 0.4 \mu\text{m}$ . The TE and TM-polarized probe light beam is incident on the upper layer of the glass cell at incident angle  $\theta_i$ .  $\delta_p^+$  and  $\delta_p^-$  indicate the transverse displacements for right- and left-circular polarization components, respectively. (b) Energy level diagram of the five-level atomic system that acts as combined Tripod and  $\Lambda$  system known as CTL-model. (c) The equivalent four-level diagram uses internal dark and bright states.

parency (EIT) [32, 33], lasing without inversion [34], low and ultraslow light propagation [35, 36], stationary light [37], light storage [38, 39], amplified nonlinear optical effects [40, 41], GH shift [42], and so on. In most of these studies, the coherent atomic medium is considered a three-level  $\Lambda$ ,  $V$ , ladder, and four-level  $N$ -type energy level structure. Recently, a novel atom-light coupling scheme, known as the combined tripod and  $\Lambda$  (CTL) scheme, was introduced for electromagnetically induced transparency (EIT) and slow light [43]. Changing the amplitudes and phases of the control fields transforms the CTL system into both  $\Lambda$  and  $N$ -type systems. This closed-loop control field structure makes the CTL system a versatile model for achieving multiple interaction pathways and quantum interference effects within the same atomic ensemble. Recent studies explored EIT [43], structure light detection [44], and GH shift [45] in the CTL atomic system.

In this paper, we investigate the tunability of the PSHE using a CTL atomic system within the cavity quantum electrodynamics (QED). The CTL configuration exhibits multiple transparency windows, providing an opportunity to achieve a tunable PSHE over a wider range of probe field detuning. In the  $\Lambda$ -type system, the PSHE exhibits behavior resembling the CTL configuration at probe field resonance. The CTL and  $\Lambda$  systems exhibit enhanced PSHE due to zero absorption and dispersion at probe field resonance. Furthermore, atomic density and amplitude of control fields do not influence PSHE at probe field resonance. In the  $N$ -type system,

the atomic density and the control field strength play a significant role in modulating the PSHE at probe field resonance. At lower atomic densities, the PSHE is enhanced, unlike in the CTL and  $\Lambda$  configurations, where atomic density has no impact on the PSHE. Importantly, the results obtained from this study are equally valid and applicable to direct  $\Lambda$ -type and  $N$ -type atomic systems, making the findings broadly relevant in cavity QED.

The rest of the paper is organized as follows: Section II presents a detailed theoretical model, and Section III discusses the results and analysis of the CTL,  $\Lambda$ -type, and  $N$ -type configurations. Finally, the conclusions are summarized in Section IV.

## II. ATOMIC MODEL AND EQUATIONS

We consider the atomic sample injected from the bottom nozzle into an ultra-high vacuum glass vapor cell made of Pyrex as shown in Fig 1(a). Atomic vapors follow  $d = 0.4 \mu\text{m}$  flow path structure i.e., the inner thickness of glass cell containing the atomic vapors. The upper and lower layers of the pyrex glass cell have permittivity  $\epsilon_1 = \epsilon_3 = 2.25$  while inside the five-level atomic medium has permittivity  $\epsilon_2$ . [46]. We consider that a TE and TM-polarized probe light beam is incident on the upper surface of the glass cell at incident  $\theta_i$ . This monochromatic Gaussian probe beam will be reflected at the structure interface or pass through the structure. In the reflection geometry, for a TM polarized Gaussian beam reflected by the interface, the field amplitudes of two circular components of reflected light can be expressed as [47]:

$$E_r^\pm \propto \frac{w_0}{w} \exp\left[-\frac{x_r^2 + y_r^2}{w}\right] \times \left[ r_p - \frac{2ix_r}{k_0w} \frac{\partial r_p}{\partial \theta_i} \mp \frac{2y_r \cot \theta_i}{k_0w} (r_p + r_s) \right]. \quad (1)$$

Here,  $w = w_0 \left[ 1 + (2\Lambda_r/k_0w_0^2)^2 \right]^{1/2}$  with beam waist  $w_0$  and Rayleigh range  $\Lambda_r = \pi w_0^2/\lambda$ . Here,  $k_0 = 2\pi/\lambda$  denotes the incident wave vector with  $\lambda$  being the light wavelength. The reflected light coordinate system is  $(x_r, y_r, z_r)$ , where superscript  $\pm$  denotes left-hand circularly polarized (LHCP) and right circularly polarized (RHCP) photon states. The complex reflection coefficients for TM polarized  $r_p$  and TE-polarized  $r_s$  can be written as [48, 49]

$$r_{p,s} = \frac{r_{p,s}^{12} + r_{p,s}^{23} e^{2ik_{z2}d}}{1 + r_{p,s}^{12} r_{p,s}^{23} e^{2ik_{z2}d}}. \quad (2)$$

where  $r_{p,s}^{ij}$  is the Fresnel's reflection coefficient at the  $i$ - $j$  interface (here  $i, j = 1, 2, 3$ ). For TM polarized

$$r_p^{ij} = \frac{k_{iz}/\epsilon_i - k_{jz}/\epsilon_j}{k_{iz}/\epsilon_i + k_{jz}/\epsilon_j}, \quad (3)$$

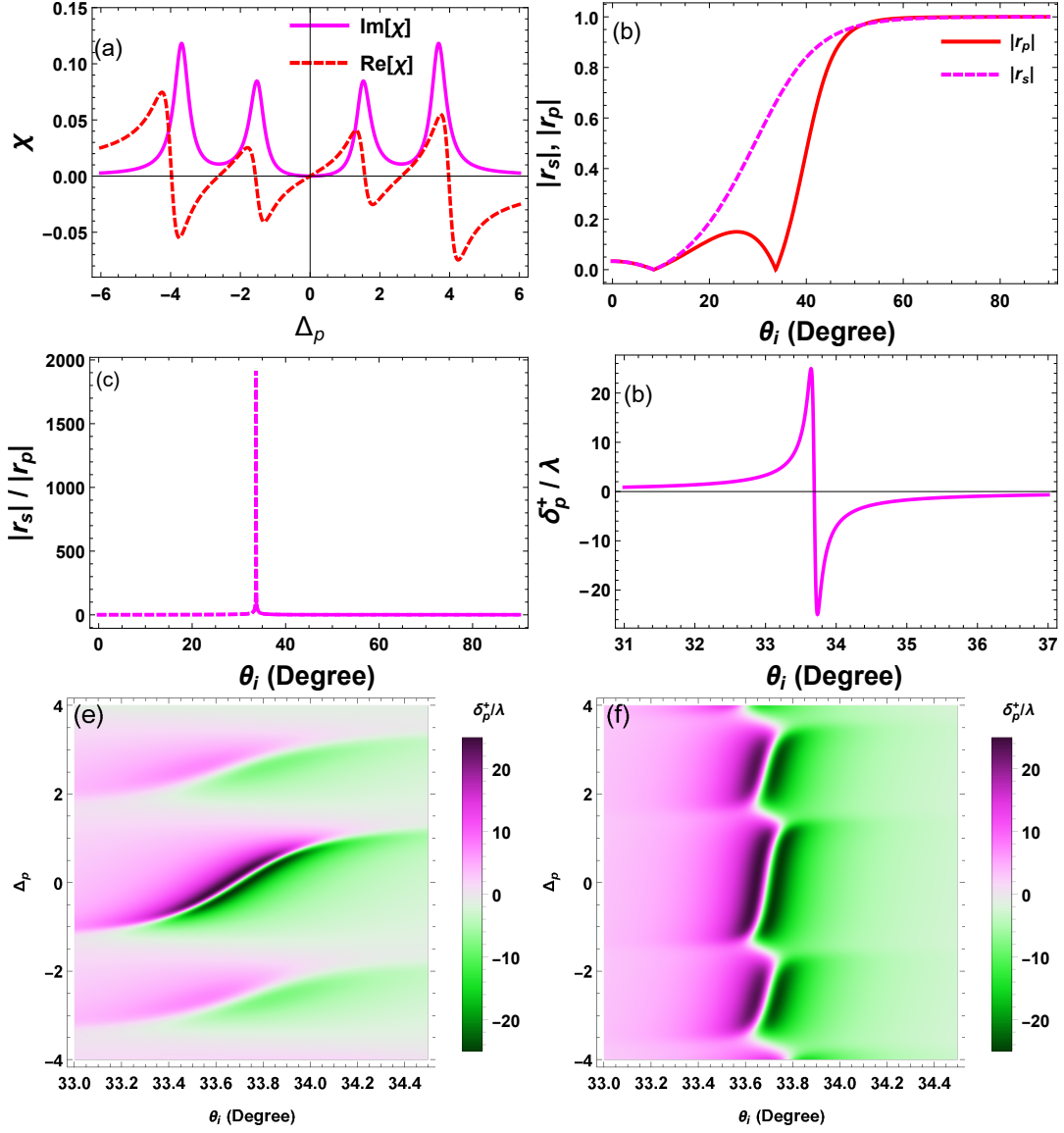


FIG. 2. (a) The absorption (solid curve) and dispersion (dashed curve) characteristics of CTL atomic system as a function of probe field detuning at  $|\Omega_1| = 1.5\gamma$ ,  $|\Omega_2| = 3\gamma$ ,  $|\Omega_3| = 2.5\gamma$ ,  $|\Omega_4| = 0.9\gamma$ ,  $\phi = 0$ , and  $\eta = 0.1\gamma$ . (b) Fresnel coefficient  $|r_s|$  and  $|r_p|$  as a function of incident angle  $\theta_i$  while (c) shows their respective ratio. (d) PSHE changing sign from positive to negative around the angle at which the ratio  $|r_s|/|r_p|$  is maximum. (e) Density plot of PSHE as a function of probe field detuning  $\Delta_p$  and incident angle  $\theta_i$  while (f) is density plot when density reduces one order of magnitude at  $\eta = 0.01\gamma$ .

and TE polarized

$$r_s^{ij} = \frac{k_{iz} - k_{jz}}{k_{iz} + k_{jz}}. \quad (4)$$

Here  $k_{iz} = \sqrt{k_0^2 \epsilon_i - k_x^2}$  represents the normal wave vector in the corresponding layer, and  $k_x = \sqrt{\epsilon_1} k_0 \sin \theta_i$  is the wave vector along the  $x$  direction.

It can be seen from Eq. (3) and Eq. (4) that the reflection coefficients depend on the permittivity of each layer. The upper and lower surface of the Pyrex glass cell has permittivities of 2.25. The permittivity of the atomic medium is related to its susceptibility by relation  $\epsilon_2 = 1 + \chi$ . The equivalent refractive index is defined as

$n = \sqrt{1 + \chi}$ . Here,  $\chi$  represents the dielectric susceptibility of the atomic medium inside the glass cell and can be expressed as  $\chi = \chi_1 + i\chi_2$ . Here, the real part ( $\chi_1$ ) represents the dispersion and the imaginary part ( $\chi_2$ ) represents the absorption of the probe field. In our model, permittivity  $\epsilon_2$  can be effectively controlled by manipulating  $\chi$ . This leads to a controllable PSHE of light. The transverse displacements can be computed as [47]

$$\delta_p^\pm = \frac{\iint y_r |E_r^\pm(x_r, y_r, z_r)|^2 dx_r dy_r}{\int |E_r^\pm(x_r, y_r, z_r)|^2 dx_r dy_r} \quad (5)$$

Utilizing the first-order Taylor series expansion of the

Fresnel reflection coefficients, the corresponding transverse spin-displacements  $\delta_p^+$  and  $\delta_p^-$  can be expressed in terms of the reflective coefficients of the three-layer atomic system [48, 50]:

$$\delta_p^\pm = \mp \frac{k_1 w_0^2 \operatorname{Re} \left[ 1 + \frac{r_s}{r_p} \right] \cot \theta_i}{k_1^2 w_0^2 + \left| \frac{\partial \ln r_p}{\partial \theta_i} \right|^2 + \left| \left( 1 + \frac{r_s}{r_p} \right) \cot \theta_i \right|^2}, \quad (6)$$

with  $k_1 = \sqrt{\varepsilon_1} k_0$ . Equation. 6 indicates that the transverse spin-dependent PSHE strongly depends on the reflectance intensity ratio  $|r_s|/|r_p|$ . A larger ratio will result in a larger PSHE and vice versa. We only presented the transverse shift of the right circularly polarized photon spin-dependent component  $\delta_p^+$  because the beam shifts for the two circular components are equal in magnitude and opposite in sign.

We consider a five-level atomic system to obtain the dielectric susceptibility of the intra-cavity medium. The energy level diagram of the five-level atomic system is shown in Fig. 1(b), which consists of three ground states,  $|a\rangle$ ,  $|c\rangle$ ,  $|d\rangle$ , and two excited states  $|b\rangle$  and  $|e\rangle$ . This five-level system combines tripod and  $\Lambda$  (CTL) subsystems. The Tripod subsystem consists of three ground states,  $|a\rangle$ ,  $|c\rangle$ ,  $|d\rangle$ , and an excited state  $|b\rangle$ , while the three-level  $\Lambda$  subsystem consists of two ground states,  $|c\rangle$  and  $|d\rangle$ , and an excited state  $|e\rangle$ . The probe field of the Rabi frequency  $\Omega_p$  is applied to the transition  $|a\rangle \rightarrow |b\rangle$ , the four control fields of Rabi frequencies  $\Omega_1$ ,  $\Omega_2$ ,  $\Omega_3$ , and  $\Omega_4$  established the connection between transition  $|b\rangle \rightarrow |c\rangle$ ,  $|b\rangle \rightarrow |d\rangle$ ,  $|e\rangle \rightarrow |c\rangle$ , and  $|e\rangle \rightarrow |d\rangle$ , respectively. The Rabi frequencies of the control fields are complex and defined as  $\Omega_j = |\Omega_j| e^{i\phi_j}$  with  $j = 1, 2, 3, 4$ . Here,  $|\Omega_j|$  is the amplitude and  $\phi_j$  is the phase of the  $j^{\text{th}}$  control field. Two distinct pathways  $|b\rangle \rightarrow |c\rangle \rightarrow |e\rangle$  and  $|b\rangle \rightarrow |d\rangle \rightarrow |e\rangle$  connect the two excited states  $|b\rangle$  and  $|e\rangle$ . This connection creates

a closed four-level coherent control coupling scheme by defining the relative phase  $\phi = (\phi_1 - \phi_2) - (\phi_3 - \phi_4)$ . The total interaction picture Hamiltonian of the system becomes

$$H = -\Omega_p^* |a\rangle \langle b| - \Omega_1^* |c\rangle \langle b| - \Omega_2^* |d\rangle \langle b| - \Omega_3^* |c\rangle \langle e| - \Omega_4^* |d\rangle \langle e| - H.c. \quad (7)$$

The two ground states  $|c\rangle$  and  $|d\rangle$  of the  $\Lambda$  subsystem form the internal dark state  $|D\rangle = (\Omega_4 |c\rangle - \Omega_3 |d\rangle)/\Omega$  and the bright state  $|B\rangle = (\Omega_3 |c\rangle + \Omega_4 |d\rangle)/\Omega$ . Here,  $\Omega = \sqrt{|\Omega_3|^2 + |\Omega_4|^2}$  is the total Rabi frequency. In terms of internal dark and bright state, the total Hamiltonian transforms:

$$H = -\Omega_p^* |a\rangle \langle b| - \beta |D\rangle \langle b| - \alpha |B\rangle \langle b| - \Omega |B\rangle \langle e| + H.c. \quad (8)$$

The parameters  $\alpha$ , and  $\beta$  are defined as;

$$\alpha = \frac{1}{\Omega} (\Omega_1^* \Omega_3^* + \Omega_2^* \Omega_4^*). \quad (9)$$

$$\beta = \frac{1}{\Omega} (\Omega_1^* \Omega_4^* - \Omega_2^* \Omega_3^*), \quad (10)$$

The equivalent energy level diagram in transforming internal dark and bright states is shown in Fig. 1 (c).

Next, we calculate the matrix element  $\rho_{ba}$  using the density matrix approach [51], which represents the optical coherence associated with the probe transition from  $|a\rangle$  to  $|b\rangle$ . As the probe field is assumed to be significantly weaker than the control fields, most of the atomic population resides in the ground state  $|a\rangle$ , allowing us to treat the probe field as a perturbation. We assume all the control fields at resonance with the respective transition. Under slowly varying amplitude and steady-state conditions, the obtained density matrix element  $\rho_{ba}$  becomes [43]

$$\rho_{ba} = \frac{\Delta_p (-|\Omega|^2 + i\Delta_p (\gamma_e/2 - i\Delta_p))}{i\Delta_p (\gamma_e/2 - i\Delta_p) \zeta + i|\Omega|^2 \Delta_p (\gamma_b/2 - i\Delta_p) + (\gamma_b/2 - i\Delta_p) (\gamma_e/2 - i\Delta_p) \Delta_p^2 - |\Omega|^2 |\beta|^2} \Omega_p, \quad (11)$$

where  $\zeta = |\alpha|^2 + |\beta|^2$ . We define probe field detuning as  $\Delta_p = \omega_p - \omega_{ab}$ , where  $\omega_p$  is probe field frequencies. The  $\gamma_e$  is the decay rate of the excited state  $|e\rangle$  and  $\gamma_b$  is the decay rate of the excited state  $|b\rangle$ . The optical response of the probe field is determined by the susceptibility  $\chi = \eta \rho_{ba}$  of the medium with  $\eta = N |\mu_{ba}|^2 / \epsilon_0 \hbar \Omega_p$  [51]. Here  $N$  is the number of atoms per unit volume and  $\mu_{ba}$  is the dipole moment between transition  $|b\rangle$  to  $|a\rangle$ . That indicates that  $\eta$  is the parameter controllable by atomic density and considered as an atomic density parameter throughout the paper. Therefore, the susceptibility of the five-level atomic medium and hence its permittivity  $\epsilon_2$  can be modified and controlled by changing several parameters such as the  $\eta$ ,  $\Delta_p$ ,  $\alpha$ ,  $\beta$ , and control field

Rabi frequencies.

### III. RESULTS AND DISCUSSION

This section is devoted to the numerical analyses of PSHE. To analyze PSHE, we select the fixed decay rates  $\gamma_e = \gamma_b = \gamma$  and beam waist  $w_0 = 50\lambda$ . All other parameters are scaled with  $\gamma = 1\text{MHz}$ . The parameters  $\alpha$ ,  $\beta$ ,  $\phi$  and  $\eta$  are the tunable parameters. We discuss the following three cases depending on the appropriate choice control field Rabi frequencies and their relative phase.

### A. $\alpha \neq 0$ and $\beta \neq 0$

When both  $\alpha$  and  $\beta$  are non-zero, the five-level atomic system operates as a CTL model. To achieve this, we set the asymmetric Rabi frequencies  $|\Omega_1| = 1.5\gamma$ ,  $|\Omega_2| = 3\gamma$ ,  $|\Omega_3| = 2.5\gamma$ ,  $|\Omega_4| = 0.9\gamma$ , and relative phase  $\phi = 0$ , ensuring that both  $\alpha$  and  $\beta$  are non-zero. We first examine the real and imaginary components of susceptibility as a function of probe field detuning,  $\Delta_p$ , in the CTL model. Figure 2(a) shows the real part of susceptibility with a dashed curve while the imaginary part of susceptibility with the solid curve. The imaginary part of  $\chi$  also demonstrates three transparency windows in the absorption spectrum at  $\Delta_p = 0$  and  $\Delta_p = \pm 2.6\gamma$ . Absorption and dispersion are zero at resonance  $\Delta_p = 0$  similar to the phenomenon of electromagnetic-induced transparency. At detuning values of  $\Delta_p = \pm 2.6\gamma$ , we observe another absorption window with a non-zero magnitude and zero dispersion. These results show that the refractive index,  $n = \sqrt{1 + \chi}$ , can be tuned by adjusting the probe field detuning, allowing control over the PSHE.

Next, we consider the situation when the probe field is incident at angle  $\theta_i$  as depicted in Fig. 1(a). To observe the angle around which ratio  $|r_s|/|r_p|$  is enhanced, we first show the Fresnel coefficient  $|r_s|$  and  $|r_p|$  as a function of incident angle  $\theta_i$  at  $\Delta_p = 0$ , and  $\eta = 0.1\gamma$ , as shown in Fig. 2(b). At an incident angle of  $\theta_i = 33.7^\circ$ , Fresnel coefficient  $|r_p|$  approaches zero while  $|r_s|$  maintains a finite value, significantly increasing the ratio  $|r_s|/|r_p|$ , as seen in Fig. 2(c). Figure 2(d) further shows the PSHE enhancement around  $\theta_i = 33.7$ . The PSHE switches sign from a positive peak value of  $25\lambda$  to a negative peak value  $-25\lambda$  around  $\theta_i = 33.7^\circ$ . The transverse PSHE is positive for  $\theta_i < 33.7^\circ$ , and negative for  $\theta_i > 33.7^\circ$ . This change in sign is due to the  $\pi$  phase alteration between the phases associated with Fresnel coefficient  $r_s$  and  $r_p$  [48].

To study the effect of probe field detuning on PSHE, figure 2(e) shows a density plot of the PSHE as a function of detuning and incident angle at fixed  $\eta = 0.1\gamma$ . A maximum PSHE of  $25\lambda$  appears at  $\Delta_p = 0$ , with an additional, lower-magnitude (around  $\leq 10\lambda$ ) PSHE at  $\Delta_p = \pm 2.6\gamma$  due to non-zero absorption at these detuning values. Another noteworthy effect is that the angle at which  $|r_p|$  approaches zero shifts by approximately  $\pm 1^\circ$  from  $33.7^\circ$ . Figure 2(f) shows a density plot of PSHE when the atomic density is reduced by an order of magnitude, setting  $\eta = 0.01\gamma$ . With this lower density, PSHE enhances and reaches  $20\lambda$  at  $\Delta_p = \pm 2.6\gamma$  while remaining the same value of  $25\lambda$  at  $\Delta_p = 0$ . Fig. 2(e) and (f), it is evident that at  $\Delta_p = 0$  PSHE is independent of density parameter  $\eta$  and stays to a constant value of  $\pm 25\lambda$ . At  $\Delta_p = \pm 2.6\gamma$ , reducing the atomic density minimizes probe field absorption that further enhances the PSHE. Additionally, the range of incident angles over which the PSHE changes sign from positive to negative becomes much narrower for  $\eta = 0.01\gamma$  compared with  $\eta = 0.1\gamma$ . Furthermore, PSHE at probe field

resonance is independent of control field strength as long as the EIT condition is satisfied due to zero absorption and dispersion.

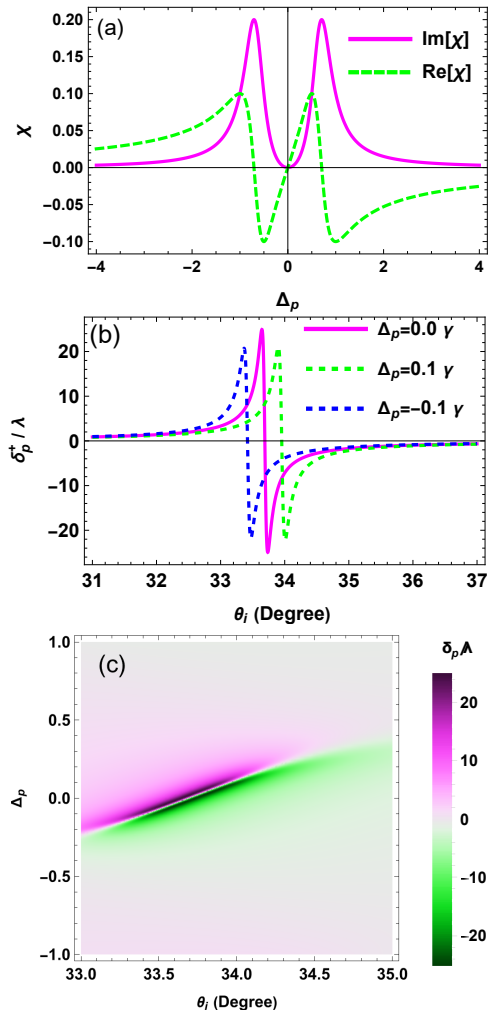


FIG. 3. (a) The absorption (solid curve) and dispersion (dashed curve) characteristics as a function of probe field detuning at  $|\Omega_1| = |\Omega_2| = 0.5\gamma$ ,  $|\Omega_3| = |\Omega_4| = 0.7\gamma$ ,  $\phi = 0$  and  $\eta = 0.1\gamma$ . These symmetric Rabi frequency values create the situation  $\alpha = 0$  and  $\beta \neq 0$ . As a result, the atomic system becomes an effective  $\Lambda$  system showing the EIT-like characteristics of the probe field. (b) PSHE as a function of probe field incident angle at three different values of  $\Delta_p$ . (c) Two-dimensional density plot of PSHE as a function of probe field detuning and incident angle at  $\eta = 0.1\gamma$ .

### B. $\alpha = 0$ and $\beta \neq 0$

When  $\alpha$  is zero and  $\beta$  is non-zero, the five-level atomic system transforms to a conventional  $\Lambda$ -type configuration. This change is due to the decoupling of levels  $|B\rangle$  and  $|e\rangle$ , as shown in Fig. 1(c). To achieve  $\alpha = 0$  and  $\beta \neq 0$ , we consider a symmetric setup with  $|\Omega_1| = |\Omega_2| = 0.5\gamma$  and  $|\Omega_3| = |\Omega_4| = 0.7\gamma$ , and set the relative phase to  $\phi = \pi$ . Figure 3(a) illustrates the sus-

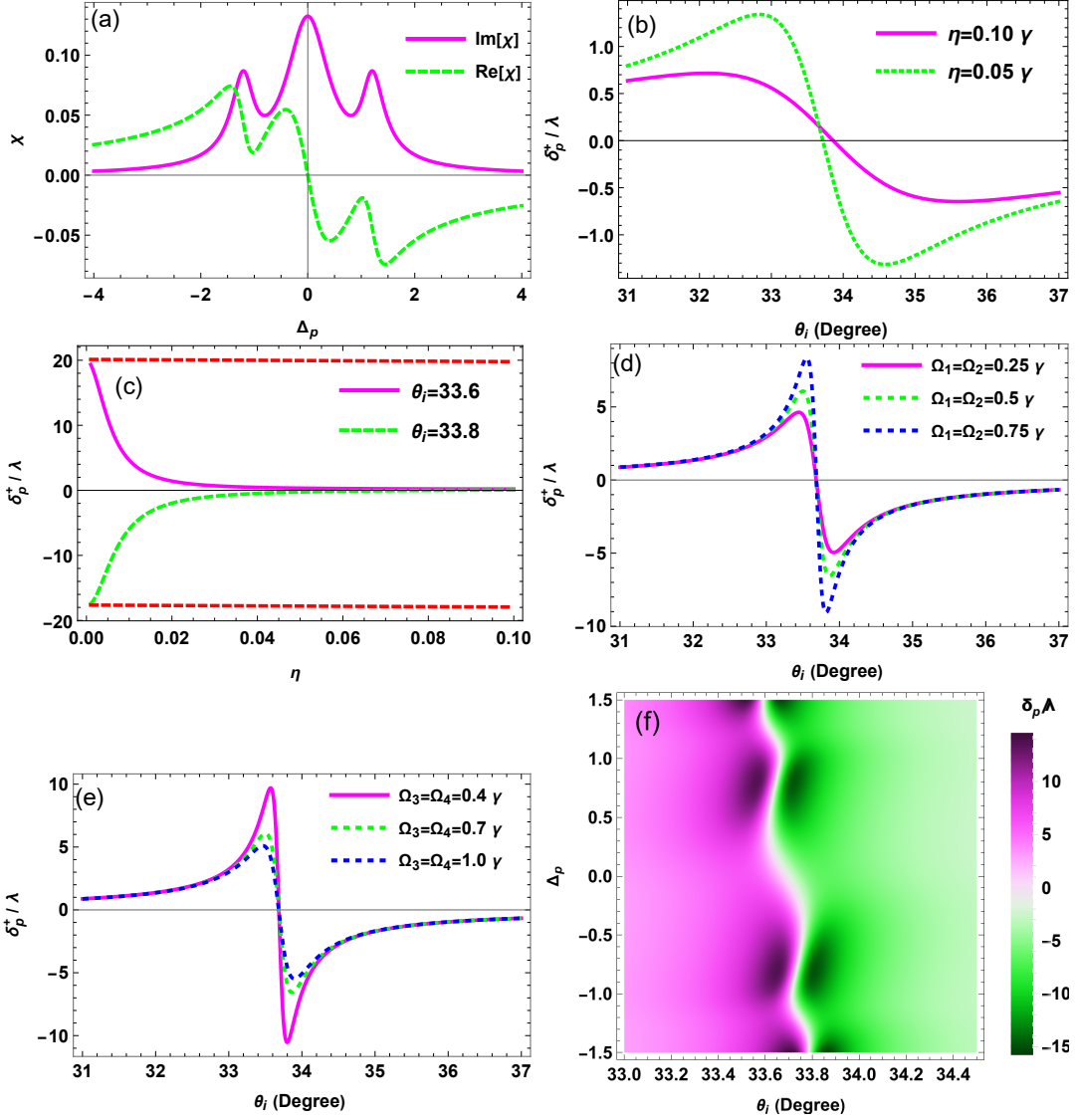


FIG. 4. (a) The absorption (solid curve) and dispersion (dashed curve) characteristics as a function of probe field detuning at  $|\Omega_1| = |\Omega_2| = 0.5\gamma$ ,  $|\Omega_3| = |\Omega_4| = 0.7\gamma$ ,  $\phi = \pi$ , and  $\eta = 0.1\gamma$ . These symmetric control field values create the situation  $\alpha \neq 0$  and  $\beta = 0$  and the atomic system becomes effectively a  $N$  type. (b) PSHE as a function of the incident angle at  $\Delta_p = 0$  at two different values of  $\eta = 0.1\gamma$  and  $\eta = 0.05\gamma$ . (c) PSHE dependence on density parameter  $\eta$  at  $\Delta_p = 0$  and at two different values of incident angles. The horizontal dotted line shows no dependence on  $\eta$  for CTL and EIT cases. (d) PSHE as a function of the incident angle at  $\Delta_p = 0$  at three different values of  $|\Omega_1| = |\Omega_2|$  whereas (e) is at three different values of  $|\Omega_3| = |\Omega_4|$ . (f) Two-dimensional plot of PSHE as a function of incident angle and probe field detuning.

ceptibility as a function of probe field detuning. This spectral response reflects the standard characteristics of electromagnetic-induced transparency (EIT) and slow light, where the intracavity medium displays EIT with normal dispersion. The plots of  $|r_s|$ ,  $|r_p|$ , and  $|r_s|/|r_p|$  show a similar trend to the CTL case and are not presented for simplicity. The solid curve in Fig. 3(b) shows that the PSHE behavior at  $\Delta_p = 0$  is identical to that of the CTL atomic configuration. Because, in both cases, the corresponding refractive index is unity with total  $\chi = 0$ . However, in the nearby region around resonance at  $\Delta_p = 0$ , the refractive index varies with detuning due to changes in susceptibility. The dashed and dotted

curves illustrate the PSHE at detunings of  $\Delta_p = 0.1\gamma$  and  $\Delta_p = -0.1\gamma$ , respectively, showing the shift in the angle at which the PSHE changes sign from positive to negative. To further analyze these findings, Fig. 3(e) presents a density plot of the PSHE versus incident angle  $\theta_i$  and probe field detuning  $\Delta_p$ . In contrast to the CTL case, significant PSHE enhancement is limited to the resonance region around  $\Delta_p = 0$  due to a single transparency window. Thus, PSHE is enhanced at zero probe field detuning similar to the CTL case. This PSHE is independent of the control field strength and atomic density as long as the EIT condition holds. In other words, the complex CTL-type system and the sim-

pler  $\Lambda$ -type system exhibit similar PSHE characteristics at probe field resonance.

### C. $\alpha \neq 0$ and $\beta = 0$

When  $\alpha$  is non-zero and  $\beta$  is zero, the five-level atomic system behaves as a conventional  $N$ -type atomic system due to the decoupling of level  $|D\rangle$ , as shown in Fig. 1(c). To achieve this condition ( $\alpha \neq 0$  and  $\beta = 0$ ), we set up a symmetric configuration with  $|\Omega_1| = |\Omega_2| = 0.5\gamma$  and  $|\Omega_3| = |\Omega_4| = 0.7\gamma$ , while keeping a relative phase of  $\phi = 0$ . Figure 4(a) displays the susceptibility as a function of the probe field detuning. Unlike the CTL and EIT cases, the dispersion is zero while absorption remains non-zero at resonance  $\Delta_p = 0$ . The plots of  $|r_s|$ ,  $|r_p|$ , and the ratio  $|r_s|/|r_p|$  follow trends similar to the CTL and EIT cases, so they are omitted here for simplicity. However, it is worth noting that the peak value of the ratio  $|r_s|/|r_p|$  is nearly two orders of magnitude smaller and exhibits a broader full-width at half maximum.

In Fig. 4(b), PSHE is shown as a function of the incident angle at  $\Delta_p = 0$  for two atomic density parameters  $\eta = 0.1\gamma$  (solid curve) and  $\eta = 0.05\gamma$  (dashed curve). Compared to the CTL and EIT cases, the magnitude of PSHE is smaller, and the range of angles where the sign changes is less steep. For the lower density,  $\eta = 0.05\gamma$ , the PSHE is larger than at  $\eta = 0.1\gamma$ . To further analyze this effect, Fig. 4(c) shows PSHE as a function of atomic density  $\eta$  at two fixed incident angles:  $\theta_i = 33.6^\circ$  (corresponding to the maximum positive shift) and  $\theta_i = 33.7^\circ$  (corresponding to the minimum shift). As the atomic density parameter  $\eta$  increases, absorption also increases. This leads to an enhancement of the imaginary part of the susceptibility. As a result, the  $|r_s|/|r_p|$  ratio is reduced, leading to a decrease in PSHE. Therefore, a lower atomic density is more suitable for enhancing PSHE in an  $N$ -type atomic system at  $\Delta_p = 0$ . This contrasts with the EIT and CTL cases at resonance, where atomic density does not affect PSHE, as indicated by the horizontal lines in Fig. 4(c). We fix  $\eta = 0.01\gamma$  in the rest of this section unless stated otherwise.

Next, we explore how varying the Rabi frequencies of the control fields affects PSHE, ensuring that  $\alpha$  and  $\Omega$  remain nearly comparable so that the system stays in an  $N$ -type configuration. First, we fix  $|\Omega_3| = |\Omega_4| = 0.7\gamma$  and vary  $|\Omega_1| = |\Omega_2|$ . The solid, dotted, and dashed curves in Fig. 4(d) represent the PSHE as a function of the incident angle for  $|\Omega_1| = |\Omega_2| = 0.25\gamma$ ,  $|\Omega_1| = |\Omega_2| = 0.5\gamma$ , and  $|\Omega_1| = |\Omega_2| = 0.75\gamma$ , respectively. The results show that PSHE increases with increase of the control field strength  $|\Omega_1| = |\Omega_2|$ . We then set  $|\Omega_1| = |\Omega_2| = 0.5\gamma$  and vary  $|\Omega_3| = |\Omega_4|$ . The solid, dotted, and dashed curves in Fig. 4(e) display the behavior of PSHE as a function of the incident angle for  $|\Omega_3| = |\Omega_4| = 0.4\gamma$ ,  $|\Omega_3| = |\Omega_4| = 0.7\gamma$ , and  $|\Omega_3| = |\Omega_4| = 1.0\gamma$ , respectively. In this case, PSHE increases as the control field  $|\Omega_3| = |\Omega_4|$  decreases. These results are different than the CTL and EIT cases, where control

field amplitude does not influence PSHE at resonance.

Finally, the two-dimensional density plot in Fig. 4(f) shows PSHE as a function of probe field detuning and incident angle. PSHE reaches higher values at  $\Delta_p \approx \pm 1\gamma$  than at  $\Delta_p = 0$ . This increase is due to two lower absorption dips at  $\Delta_p \approx \pm 1\gamma$  than at  $\Delta_p = 0$ , as seen in the susceptibility curve in Fig. 4(a). This behavior contrasts with the CTL case, where PSHE smoothly decreases as it moves away from the resonance point  $\Delta_p = 0$ . Overall, the magnitude of PSHE is lower at  $\Delta_p = 0$  and higher at  $\Delta_p \neq 0$ , while in the CTL case, it behaves oppositely, as evidenced by comparing these results with Fig. 2(e).

## IV. CONCLUSION

In conclusion, we studied the PSHE of a probe field induced by four coherent control fields. These control fields form a combined tripod and  $\Lambda$  configuration. By appropriately selecting the amplitudes and phases of the control fields, a five-level atomic system can be transformed into  $\Lambda$  and  $N$ -type atomic configurations. We demonstrated that the PSHE can be tuned via probe field detuning, the magnitudes of the control field Rabi frequencies, and atomic density. At resonance, the CTL and  $\Lambda$  configurations exhibited similar behavior, showing no dependence on atomic density or control field strengths and enhanced PSHE. However, unlike the  $\Lambda$  system, the CTL system displayed enhanced PSHE at multiple probe field detunings. For the  $N$ -type system, the PSHE across all probe field detunings depends on atomic density and control field strength, providing greater tunability with a wider range of adjustable parameters.

It is worth noting that the  $\Lambda$  and  $N$ -type atomic configurations considered here are limiting cases derived from the CTL configuration. The results presented for  $\Lambda$  and  $N$ -type atomic systems are also applicable to natural  $\Lambda$  and  $N$ -type atomic structures by simply turning off the unnecessary control fields making our finding quite general for  $\Lambda$  and  $N$ -type atomic system. Our proposed results may be detected in the experiment by incorporating standard weak measurement protocol [52] on Rubidium or Cesium Hyperfine energy levels. It is worth noting that the experimental realization of CTL system PSHE may be challenging due to the complexity of four control fields compare to the direct  $\Lambda$  and  $N$ -type system. The flexible tunability of the spin-dependent splitting of light may have potential applications in cavity QED devices.

## V. ACKNOWLEDGMENTS

M. Shah acknowledges financial support from the postdoctoral research grant YS304023905.

- 
- [1] J. Sinova, S. O. Valenzuela, J. Wunderlich, C. H. Back, and T. Jungwirth, Spin Hall effects, *Rev. Mod. Phys.* **87**, 1213 (2015).
- [2] B. A. Bernevig and S.-C. Zhang, Quantum spin Hall effect, *Phys. Rev. Lett.* **96**, 106802 (2006).
- [3] T. Jungwirth, J. Wunderlich, and K. Olejník, Spin Hall effect devices, *Nature materials* **11**, 382 (2012).
- [4] J. E. Hirsch, Spin Hall effect, *Phys. Rev. Lett.* **83**, 1834 (1999).
- [5] Y. K. Kato, R. C. Myers, A. C. Gossard, and D. D. Awschalom, Observation of the spin Hall effect in semiconductors, *Science* **306**, 1910 (2004).
- [6] C. L. Kane and E. J. Mele, Quantum spin Hall effect in graphene, *Phys. Rev. Lett.* **95**, 226801 (2005).
- [7] C. Safeer, J. Ingla-Aynés, F. Herling, J. H. Garcia, M. Vila, N. Ontoso, M. R. Calvo, S. Roche, L. E. Hueso, and F. Casanova, Room-temperature spin Hall effect in graphene/mos2 van der waals heterostructures, *Nano Letters* **19**, 1074 (2019).
- [8] A. Kavokin, G. Malpuech, and M. Glazov, Optical spin hall effect, *Phys. Rev. Lett.* **95**, 136601 (2005).
- [9] M. Kim, Y. Yang, D. Lee, Y. Kim, H. Kim, and J. Rho, Spin Hall effect of light: from fundamentals to recent advancements, *Laser & Photonics Reviews* **17**, 2200046 (2023).
- [10] L. Sheng, Y. Chen, S. Yuan, X. Liu, Z. Zhang, H. Jing, L.-M. Kuang, and X. Zhou, Photonic spin hall effect: Physics, manipulations, and applications, *Progress in Quantum Electronics* **91-92**, 100484 (2023).
- [11] S. Liu, S. Chen, S. Wen, and H. Luo, Photonic spin hall effect: fundamentals and emergent applications, *Opto-Electronic Science* **1**, 220007 (2022).
- [12] J.-M. Mnard, A. E. Mattacchione, M. Betz, and H. M. V. Driel, Imaging the spin Hall effect of light inside semiconductors via absorption, *Opt. Lett.* **34**, 2312 (2009).
- [13] X. Zhou, X. Ling, H. Luo, and S. Wen, Identifying graphene layers via spin Hall effect of light, *Appl. Phys. Lett.* **101**, 251602 (2012).
- [14] L. Cai, M. Liu, S. Chen, Y. Liu, W. Shu, H. Luo, and S. Wen, Quantized photonic spin Hall effect in graphene, *Phys. Rev. A* **95**, 013809 (2017).
- [15] M. Shah, M. Shah, N. A. Khan, M. Sajid, M. Jan, and G. Xianlong, Tunable quantized spin Hall effect of light in graphene, *Results in Physics* **60**, 107676 (2024).
- [16] L. Salasnick, Enhancement of four reflection shifts by a three-layer surface-plasmon resonance, *Phys. Rev. A* **86**, 055801 (2012).
- [17] X. Zhou and X. Ling, Enhanced photonic spin Hall effect due to surface plasmon resonance, *IEEE Photonics J.* **8**, 1 (2016).
- [18] X.-J. Tan and X.-S. Zhu, Enhancing photonic spin Hall effect via long-range surface plasmon resonance, *Opt. Lett.* **41**, 2478 (2016).
- [19] Y. Xiang, X. Jiang, Q. You, J. Guo, and X. Dai, Enhanced spin Hall effect of reflected light with guided-wave surface plasmon resonance, *Photon. Res., PRJ* **5**, 467 (2017).
- [20] R.-G. Wan and M. S. Zubairy, Controlling photonic spin Hall effect based on tunable surface plasmon resonance with an n-type coherent medium, *Phys. Rev. A* **101**, 033837 (2020).
- [21] X. Yin, Z. Ye, J. Rho, Y. Wang, and X. Zhang, Photonic spin Hall effect at metasurfaces, *Science* **339**, 1405 (2013).
- [22] M. Kim, D. Lee, Y. Yang, Y. Kim, and J. Rho, Reaching the highest efficiency of spin Hall effect of light in the near-infrared using all-dielectric metasurfaces, *Nat Commun* **13**, 2036 (2022).
- [23] M. Shah and M. Sajid, Surface states-dependent giant quantized photonic spin Hall effect in a magnetic topological insulator thin film, *Physica E Low Dimens. Syst. Nanostruct.* **138**, 115113 (2022).
- [24] G. Jia, R. Zhang, Z. Huang, Q. Ma, H. Wang, and R. Asgari, Tunable photonic spin Hall effect due to the chiral Hall effect in strained weyl semimetals, *New Journal of Physics* **23**, 073010 (2021).
- [25] P. V. Kapitanova, P. Ginzburg, F. J. Rodríguez-Fortuño, D. S. Filonov, P. M. Voroshilov, P. A. Belov, A. N. Poddubny, Y. S. Kivshar, G. A. Wurtz, and A. V. Zayats, Photonic spin Hall effect in hyperbolic metamaterials for polarization-controlled routing of subwavelength modes, *Nature Communications* **5**, 3226 (2014).
- [26] M. Shah, Probing topological quantum phase transitions via photonic spin Hall effects in spin-orbit coupled 2D quantum materials, *J. Phys. D Appl. Phys.* **55**, 105105 (2021).
- [27] W. Kort-Kamp, Topological phase transitions in the photonic spin Hall effect, *Phys. Rev. Lett.* **119**, 147401 (2017).
- [28] T. Tang, K. Shen, J. Li, X. Liang, Y. Tang, C. Li, and Y. He, Optimal weak measurement scheme for chiral molecular detection based on photonic spin Hall effect, *Opt. Express*, **31**, 40308 (2023).
- [29] T. Zhu, Y. Lou, Y. Zhou, J. Zhang, J. Huang, Y. Li, H. Luo, S. Wen, S. Zhu, Q. Gong, M. Qiu, and Z. Ruan, Generalized spatial differentiation from the spin Hall effect of light and its application in image processing of edge detection, *Phys. Rev. Appl.* **11**, 034043 (2019).
- [30] C. Imbert, Calculation and experimental proof of the transverse shift induced by total internal reflection of a circularly polarized light beam, *Physical Review D* **5**, 787 (1972).
- [31] F. Goos and H. Hnchen, Ein neuer und fundamentaler versuch zur totalreflexion, *Annalen der Physik* **436**, 333 (1947).
- [32] M. Fleischhauer, A. Imamoglu, and J. P. Marangos, Electromagnetically induced transparency: Optics in coherent media, *Reviews of modern physics* **77**, 633 (2005).
- [33] K.-J. Boller, A. Imamolu, and S. E. Harris, Observation of electromagnetically induced transparency, *Phys. Rev. Lett.* **66**, 2593 (1991).
- [34] M. O. Scully, S.-Y. Zhu, and A. Gavrielides, Degenerate quantum-beat laser: Lasing without inversion and inversion without lasing, *Physical review letters* **62**, 2813 (1989).
- [35] L. V. Hau, S. E. Harris, Z. Dutton, and C. H. Behroozi, Light speed reduction to 17 metres per second in an ultracold atomic gas, *Nature* **397**, 594 (1999).
- [36] D. Budker, D. Kimball, S. Rochester, and V. Yashchuk, Nonlinear magneto-optics and reduced group velocity of light in atomic vapor with slow ground state relaxation, *Physical review letters* **83**, 1767 (1999).



- [37] M. Bajcsy, A. S. Zibrov, and M. D. Lukin, Stationary pulses of light in an atomic medium, *Nature* **426**, 638 (2003).
- [38] D. F. Phillips, A. Fleischhauer, A. Mair, R. L. Walsworth, and M. D. Lukin, Storage of light in atomic vapor, *Physical review letters* **86**, 783 (2001).
- [39] C. Liu, Z. Dutton, C. H. Behroozi, and L. V. Hau, Observation of coherent optical information storage in an atomic medium using halted light pulses, *Nature* **409**, 490 (2001).
- [40] H. Schmidt and A. Imamoglu, Giant kerr nonlinearities obtained by electromagnetically induced transparency, *Optics letters* **21**, 1936 (1996).
- [41] M. Pack, R. Camacho, and J. C. Howell, Transients of the electromagnetically-induced-transparency-enhanced refractive kerr nonlinearity: Theory, *Physical Review A Atomic, Molecular, and Optical Physics* **74**, 013812 (2006).
- [42] Ziauddin, S. Qamar, and M. S. Zubairy, Coherent control of the goos-hänchen shift, *Physical Review A Atomic, Molecular, and Optical Physics* **81**, 023821 (2010).
- [43] H. Hamed, J. Ruseckas, and G. Juzeliūnas, Electromagnetically induced transparency and nonlinear pulse propagation in a combined tripod and  $\lambda$  atom-light coupling scheme, *Journal of Physics B: Atomic, Molecular and Optical Physics* **50**, 185401 (2017).
- [44] H. R. Hamed, V. Kudriašov, J. Ruseckas, and G. Juzeliūnas, Azimuthal modulation of electromagnetically induced transparency using structured light, *Optics Express* **26**, 28249 (2018).
- [45] M. Abbas, S. H. Asadpour, Ziauddin, P. Zhang, J. Ruseckas, and H. R. Hamed, Goos-hänchen shifts in a combined tripod and  $\lambda$  atom-light coupling scheme, *Physical Review A* **110**, 023730 (2024).
- [46] Such micro vapor cells made of quartz or Pyrex are available from Akatsuki Tech Japan. A typical value of Pyrex glass refractive index is approximately 1.5 leading to  $\epsilon \approx 2.25$ .
- [47] X.-J. Tan and X.-S. Zhu, Enhancing photonic spin Hall effect via long-range surface plasmon resonance, *Optics Letters* **41**, 2478 (2016).
- [48] M. Waseem, M. Shah, and G. Xianlong, Gain-assisted control of the photonic spin Hall effect, *Phys. Rev. A* **110**, 033104 (2024).
- [49] R.-G. Wan and M. S. Zubairy, Controlling photonic spin Hall effect based on tunable surface plasmon resonance with an n-type coherent medium, *Physical Review A* **101**, 033837 (2020).
- [50] Y. Xiang, X. Jiang, Q. You, J. Guo, and X. Dai, Enhanced spin Hall effect of reflected light with guided-wave surface plasmon resonance, *Photonics Research* **5**, 467 (2017).
- [51] M. O. Scully and M. S. Zubairy, *Quantum optics* (Cambridge university press, 1997).
- [52] H. Luo, X. Zhou, W. Shu, S. Wen, and D. Fan, Enhanced and switchable spin Hall effect of light near the Brewster angle on reflection, *Phys. Rev. A* **84**, 043806 (2011).